Article

Insights into the Photocatalytic Bacterial Inactivation by Flower-Like Bi_2WO_6 under Solar or Visible Light, Through in Situ Monitoring and Determination of Reactive Oxygen Species (ROS)

Minoo Karbasi [1,2], Fathallah Karimzadeh [1,*], Keyvan Raeissi [1], Sami Rtimi [2], John Kiwi [2], Stefanos Giannakis [3,*] and Cesar Pulgarin [2]

[1] Department of Materials Engineering, Isfahan University of Technology, Isfahan 84156-83111, Iran
[2] School of Basic Sciences (SB), Institute of Chemical Science and Engineering (ISIC), Group of Advanced Oxidation Processes (GPAO), École Polytechnique Fédérale de Lausanne (EPFL), Station 6, CH-1015 Lausanne, Switzerland
[3] Departamento de Ingeniería Civil: Hidráulica, Universidad Politécnica de Madrid (UPM), E.T.S. Ingenieros de Caminos, Canales y Puertos, Energía y Medio Ambiente, Unidad docente Ingeniería Sanitaria, c/ Profesor Aranguren, s/n, ES-28040 Madrid, Spain
* Correspondence: karimzadeh_f@cc.iut.ac.ir (F.K.); stefanos.giannakis@upm.es (S.G.)

check for updates

Abstract: This study addresses the visible light-induced bacterial inactivation kinetics over a Bi_2WO_6 synthesized catalyst. The systematic investigation was undertaken with Bi_2WO_6 prepared by the complexation of Bi with acetic acid (carboxylate) leading to a flower-like morphology. The characterization of the as-prepared Bi_2WO_6 was carried out by X-ray diffraction (XRD), scanning electron microscopy (SEM), X-ray photoelectron spectroscopy (XPS), specific surface area (SSA), and photoluminescence (PL). Under low intensity solar light (<48 mW/cm^2), complete bacterial inactivation was achieved within two hours in the presence of the flower-like Bi_2WO_6, while under visible light, the synthesized catalyst performed better than commercial TiO_2. The in situ interfacial charge transfer and local pH changes between Bi_2WO_6 and bacteria were monitored during the bacterial inactivation. Furthermore, the reactive oxygen species (ROS) were identified during *Escherichia coli* inactivation mediated by appropriate scavengers. The ROS tests alongside the morphological characteristics allowed the proposition of the mechanism for bacterial inactivation. Finally, recycling of the catalyst confirmed the stable nature of the catalyst presented in this study.

Keywords: flower-like Bi_2WO_6; *E.coli* inactivation; reactive oxygen species (ROS); photocatalysis; solar disinfection; water treatment; pollution

1. Introduction

Over the last few decades, environmental contamination has shifted from the exclusive focus of organic and inorganic pollutants [1], towards the inclusion of bacteria and other organisms [2–4]. Therefore, well-organized methods are urgently required to control the spread [5] or eradicate microorganism-related issues [6]. In recent times, beside the traditional bacterial inactivation methods such as UV disinfection and chlorination, a green, efficient, and cost-effective semiconductor photocatalysis has appeared to be a more promising technique [7,8]. TiO_2 has been extensively reported as an effective bactericidal semiconductor photocatalyst due to its high stability, strong redox potential, low cost, and non-toxic nature, but its band-gap of 3.2 eV allows light absorption up to 387 nm which makes up just over 4% of the total solar spectrum [9–11].

Since solar radiation contains more visible light (~47%) than UV, the appropriate use of this fraction becomes necessary through the employment of efficient visible-light photocatalysts [12]. As a promising visible-light-driven photocatalyst with good chemical and thermal stability, Bi_2WO_6, beside its non-toxic and environmentally friendly nature, is a typical n-type semiconductor composed of accumulated layers of alternating $(Bi_2O_2)^{2+}$ layers and $(WO_4)^{2-}$ octahedral sheets [13,14]. The valence band of Bi_2WO_6 consists of O 2p and Bi 6s hybrid orbitals, its narrowed band gap increases visible light absorption capacity, and photoactivity [15,16], while its photocatalytic activity greatly depends on morphology, particle size, surface area, and interface structure [17,18]. Constructing a unique micro/nano hierarchical structure usually shortens the pathways of water pollutants, absorb incidental light more efficiently, because of multiple-scattering increase, and easily separated from wastewater by filtration or sedimentation methods [13,19,20].

However, despite the long presence of this catalyst as a possible solution, most studies on Bi_2WO_6 have focused on the photocatalytic degradation of organic pollutants, with only a few studies investigating the photocatalytic inactivation of microorganisms. Ren et al. [21] reported *Escherichia coli* degradation in a few hours on Bi_2WO_6 nest-like structures in a pseudo-first order process. Helali et al. [22] prepared a 20 m^2/g SSA Bi_2WO_6 leading to *E. coli* inactivation within four to five hours under solar light on a hydrothermally grown mixture of Bi-nitrate and Na-tungstate in a 65–35% ratio while a similar study has been reported by Amano et al. [23]. However, there is a relatively wide gap in literature on effective preparation of robust structures with high specific surface areas in order to promote efficient disinfection, and a gap in interpreting the pathways to bacterial inactivation by this catalyst.

This study aims to assess a facile preparation method for flower-like Bi_2WO_6 photocatalysts destined for disinfection applications. As such, we assess the preparation parameters (aging, temperature, pH) in order to modify the structural (crystalline) and morphological characteristics (flower-like, nanoparticles). These modifications are envisioned to create a series of catalysts, and their activity under low-intensity solar or visible light will be assessed. Furthermore, the robustness of the catalyst in serial reuse cycles will be evaluated for its stability. Last but not least, special focus will be given to the identification of the pathways that lead to bacterial inactivation in an effort to decrypt the mechanistic action mode of the flower-like Bi_2WO_6.

2. Materials and Methods

2.1. Synthesis of Flower-Like Bi_2WO_6 Samples

All chemicals were of analytical grade. They were used as received without any further purification and were purchased from Merck, Germany. All solutions were prepared with Milli-Q water (18.2 MΩ cm). In a typical hydrothermal procedure for the synthesis of flower-like Bi_2WO_6, 0.5 mmol of $Na_2WO_4 \cdot 2H_2O$ was dissolved in an 80 mL solvent containing 16 mL acetic acid and 64 mL Milli-Q water until attaining a clear solution. Then, 1 mmol of $Bi(NO_3)_3 \cdot 5H_2O$ solid was added to the solution, and a white precipitate immediately emerged. Next, the reaction mixture was stirred for 1 h, transferred into a 120 mL Teflon-lined stainless-steel reactor, and heated at 160 °C for 12 h. The as-formed yellow precipitates were collected, washed with distilled water, and dried in vacuum at 70 °C for 10 h. A schematic representation of the synthesis is illustrated in Scheme 1. The influence of the hydrothermal reaction time and temperature has been explored as shown in Table 1. In order to investigate the effect of morphology on photocatalysis, Bi_2WO_6 nanoparticles (BWO6) were prepared applying the same hydrothermal method at 200 °C for 24 h by the regulation of pH to 10.
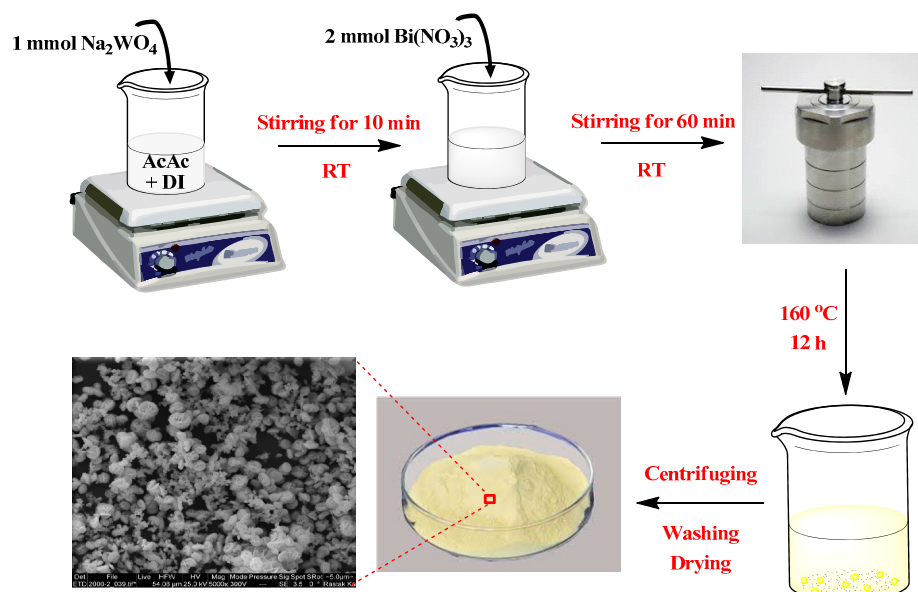
Scheme 1. Schematic illustration of the preparation of flower-like Bi_2WO_6 by hydrothermal method.

Table 1. Bi_2WO_6 obtained at the different synthetic conditions.

Samples	Reaction Time (h)	Reaction Temperature (°C)
BWO1	12	160
BWO2	18	160
BWO3	24	160
BWO4	24	180
BWO5	24	200
BWO6	24	200 (pH = 10)

2.2. Physical Characterization of the Bi_2WO_6 Flakes

The crystallinity and phase identification of the as-prepared samples were determined by powder X-ray diffraction (XRD) using an X'Pert MPD PRO (Panalytical) analyzer, equipped with a ceramic tube (Cu anode, $\lambda = 1.54060$ Å), and with a continuous scanning rate in the range of $5° < 2\theta < 80°$. The results were studied with Rietvield refinement by the FullProf program. The morphology developments of the samples were characterized using scanning electron microscopy (SEM, FEI Quanta 200). Before SEM imaging, the samples were coated with a thin layer of gold. The specific surface area and porosity size were obtained using Brunauer–Emmett–Teller (BET) analysis, performed with a BELSORP-mini II analyzer, Japan. The photoluminescence (PL) measurement was carried out using a fluorescence spectrophotometer (Perkin Elmer LS55) equipped with a xenon lamp at an excitation wavelength of $\lambda = 340$ nm. The surface atomic percentage of the element in the as-synthesized sample was analyzed using an AXIS NOVA photoelectron spectrometer with a mono-chromatic Al Ka X-ray ($h\nu = 1486.6$ eV) source (Kratos Analytical, Manchester, UK). The interfacial in situ voltage and pH variation during the bacterial inactivation was monitored in a pH/mV/Temp meter (Jenco 6230N) equipped with a microprocessor and a RS-232-C IBM interface for data recording.

2.3. Photocatalytic Antibacterial Activity on Bi_2WO_6 and Light Sources

The bacterial strain used was a wild type *E. coli* K12, supplied by the German Collection of Microorganisms and Cell Cultures, DSMZ (No. 498). The master plate and stock solution were prepared according to previous research reported by our laboratory [24,25]. The bacterial concentration

of the samples was measured in Colony Forming Units (CFU/mL) and was determined by plating on a non-selective cultivation media, namely, Plate Count Agar (PCA). A total of 1 mL of the sample was withdrawn after each interval and then serial dilutions were made in a sterile 0.8% NaCl/KCl solution. A 100 μL aliquot was pipetted onto a nutrient agar plate and processed using the standard plate count method. The plates were incubated at 37 °C followed by the bacterial evaluation. Experimental results were carried in triplicate runs applying statistical analysis for the calculation of mean and standard deviation (reported in the graphs). Samples were irradiated in the cavity of a SUNTEST solar simulator CPS (Atlas GmbH, Hanau, Germany) with an overall light irradiance of 48 mW/cm^2 (~0.8 × 10^{16} photons/s, Supplementary Figure S1). A cut-off filter was used in the SUNTEST cavity to filter the light <310 nm. A second cut-off filter was also used during bacterial inactivation under visible light with a cut-off blocking the wavelength < 405 nm rendering (Supplementary Figure S2). Finally, after the two filters, the visible light irradiance reaching the sample was 38 mW/cm^2.

3. Results

3.1. Synthesis and Characterization of Bi$_2$WO$_6$: X-Ray Diffraction (XRD), Scanning Electron Microscopy (SEM), X-Ray Photoelectron Spectroscopy (XPS), and SSA Determination

Figure 1 depicts the XRD patterns of the as-synthesized Bi$_2$WO$_6$ via the hydrothermal method at different reaction times and temperatures. All of the XRD patterns illustrated that characteristic peaks were in good agreement with the orthorhombic phased Bi$_2$WO$_6$ in the standard JCPDS card (39-0256) [26]. No other diffraction peaks arising from possible impurities were detected. With the holding time increasing to 24 h, the characteristic peaks became much sharper due to an increase in crystallinity. Understandably, the increment of the temperature with the constant reaction time for 24 h resulted in the same trend because of grain growth. Table 2 illustrates the crystallite size of the samples (using the Scherrer formula based on the half-width of their (113) peak) calculated by the Rietveld method using the FullProf program.
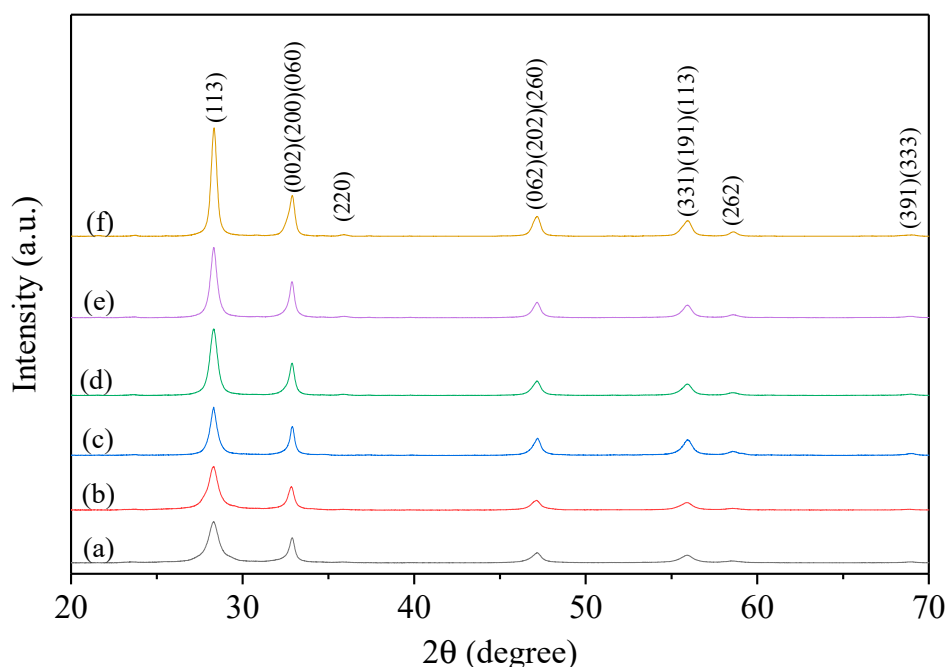

Figure 1. X-ray diffraction patterns of the Bi$_2$WO$_6$ samples: (**a**) BWO1, (**b**) BWO2, (**c**) BWO3, (**d**) BWO4, (**e**) BWO5, and (**f**) BWO6. Profiles are shifted in y-scale for clarity.
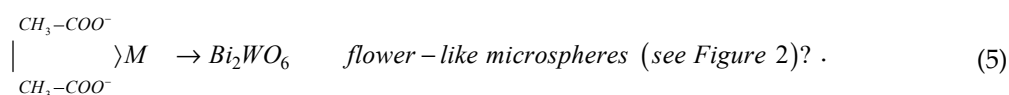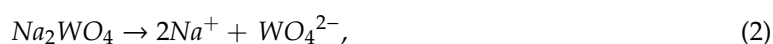
Table 2. Rietveld structural parameters of the samples.

Samples	Crystallite Size (nm)
BWO1	9
BWO2	10
BWO3	17
BWO4	20
BWO5	22
BWO6	31

The scanning electron microscopy (SEM) images of the Bi_2WO_6 samples prepared under different experimental conditions are shown in Figure 2. Heating at 160 °C for 12 h and 18 h (Figure 2a,b) led to aggregated irregular small Bi_2WO_6 nanoparticles and flower-like microspheres. However, when the heating time was prolonged to 24 h (see Figure 2c), organized hierarchical flower-like Bi_2WO_6 microspheres composed of nanoplates were obtained and the aggregated nanoparticles totally disappeared (Figure 2e,f). The SEM images of as-prepared Bi_2WO_6 nanoparticles are also shown in Figure 2f. The joint effect of nanoparticles assembly followed by the localized ripening mechanism as well as the hierarchical assembly of nanoplates have been also previously reported for the formation mechanism of flower-like microspheres [27,28]. Owing to the absence of discrete nanoplates according to the SEM images at different reaction times (Figure 2), the former mechanism seems to predominate.

Scheme 2 illustrates the proposed formation mechanism of flower-like Bi_2WO_6 microspheres. Nanoparticles initially aggregated, then the self-assembled nanoparticles preferentially grew along <010>. Longer reaction times and higher temperatures result in dissolution of some nanoplates leading concomitantly to re-deposition by Ostwald ripening [27,28].

The relevant reactions leading to the Bi_2WO_6 synthesis in aqueous solutions when working in acetic acid media can be suggested as follows:
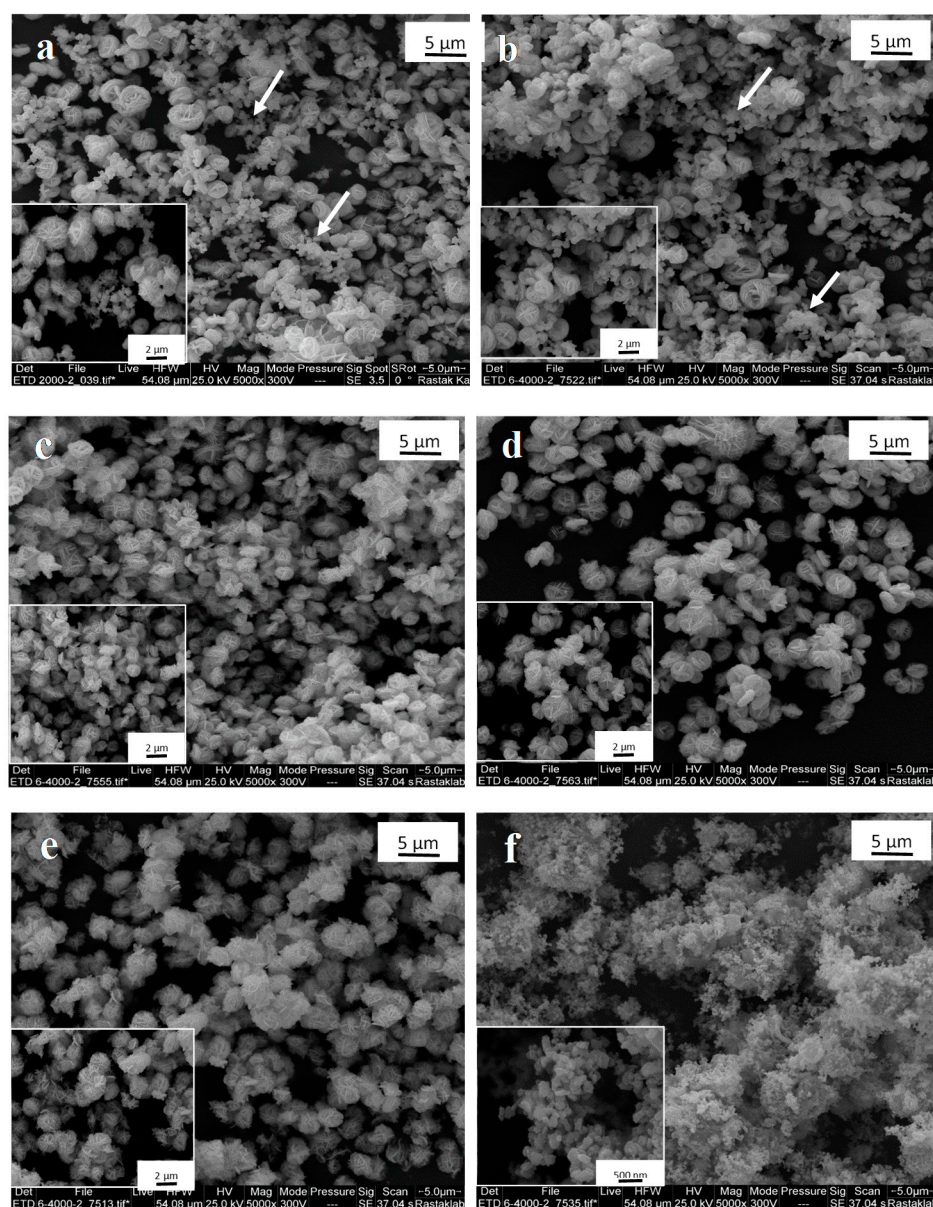
$$Bi(NO_3)_3 \rightarrow Bi^{3+} + 3NO_3{}^-, \tag{1}$$

$$Na_2WO_4 \rightarrow 2Na^+ + WO_4{}^{2-}, \tag{2}$$

$$CH_3 - COOH + H_2O \rightarrow CH_3 - COO^- + H_3O^+ \quad pK_a 4.75, \tag{3}$$

$$Bi_3{}^+ + WO_4{}^{2-} + CH_3 - COO^- \rightarrow CH_3COO^- + \left. \begin{matrix} CH_3 - COO^- \\ | \\ CH_3 - COO^- \end{matrix} \right\rangle M \ , \tag{4}$$

$$\left. \begin{matrix} CH_3 - COO^- \\ | \\ CH_3 - COO^- \end{matrix} \right\rangle M \rightarrow Bi_2WO_6 \quad flower-like\ microspheres\ \left(see\ Figure\ 2\right)? \ . \tag{5}$$
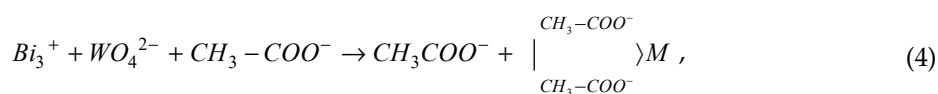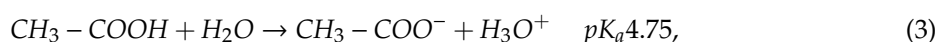
Figure 2. Scanning electron microscopy (SEM) images of Bi_2WO_6 samples prepared under different conditions: (**a**) BWO1, (**b**) BWO2, (**c**) BWO3, (**d**) BWO4, (**e**) BWO5, and (**f**) BWO6.

The initial complex between Bi and acetic acid presents a stability constant of $10^{2.6–2.7}$ [29], which is not in the range found for insoluble complexes/precipitates $>10^{11–12}$ [30–32]. This coordination complex is suggested in Equation (4) (Bi = M). The complex formation which is the precursor of Bi_2WO_6 does not lead to precipitate formation and gradually decomposes releasing Bi^{3+} which reacts with WO_4^{2-}. Therefore, the nanoplate formation leads to aggregates which present inner pores/voids and provide the required contact area for the photocatalytic bacterial inactivation.

In addition to the crystal structure and morphology, the surface chemical composition of the as-synthesized flower-like sample at 200 °C for 24 h was examined by XPS. As shown in the survey XPS spectrum in Figure 3, the Bi, O, W, and C elements were present in the pure Bi_2WO_6. The C element peak can be attributed to adventitious carbon from the sample preparation and/or the XPS instrument itself [33]. The surface atomic concentration ratio of Bi:W:O estimating from XPS peak areas is around 2.0:0.8:5.4, which further confirms its composition of Bi_2WO_6. Furthermore, the peaks centering at 164.7 and 159.4 eV are attributed to the binding energies of Bi $4f_{5/2}$ and Bi $4f_{7/2}$, respectively (inset

of Figure 3), confirming Bi^{3+} ions in the crystalline structure [34–36]. The W4f energy region can be designated to be the +6 oxidation state of tungsten in accordance with previous reports [33,36].
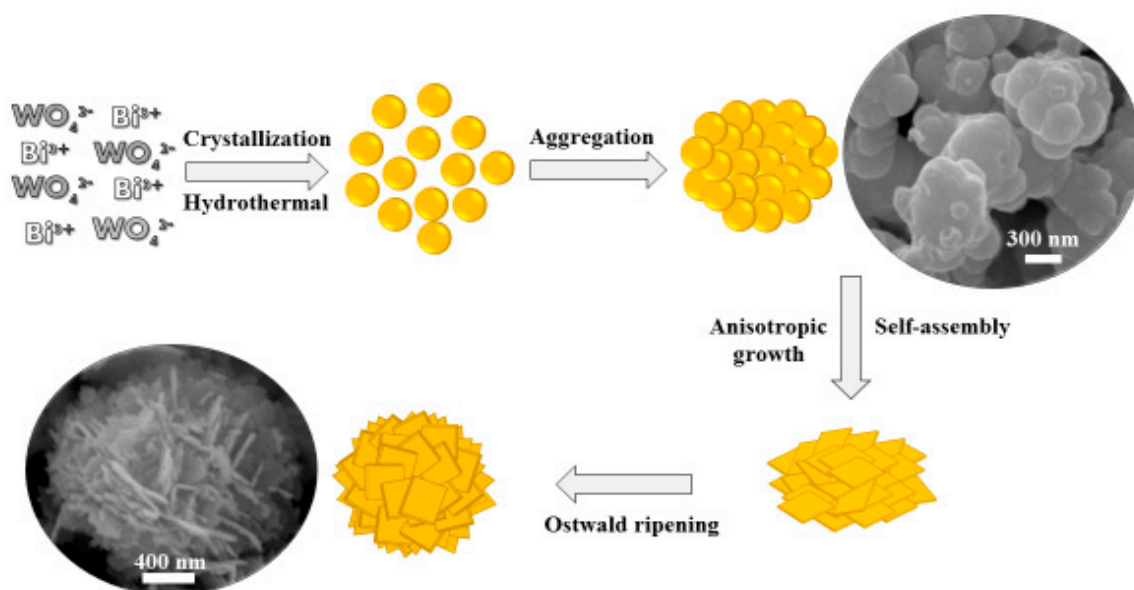
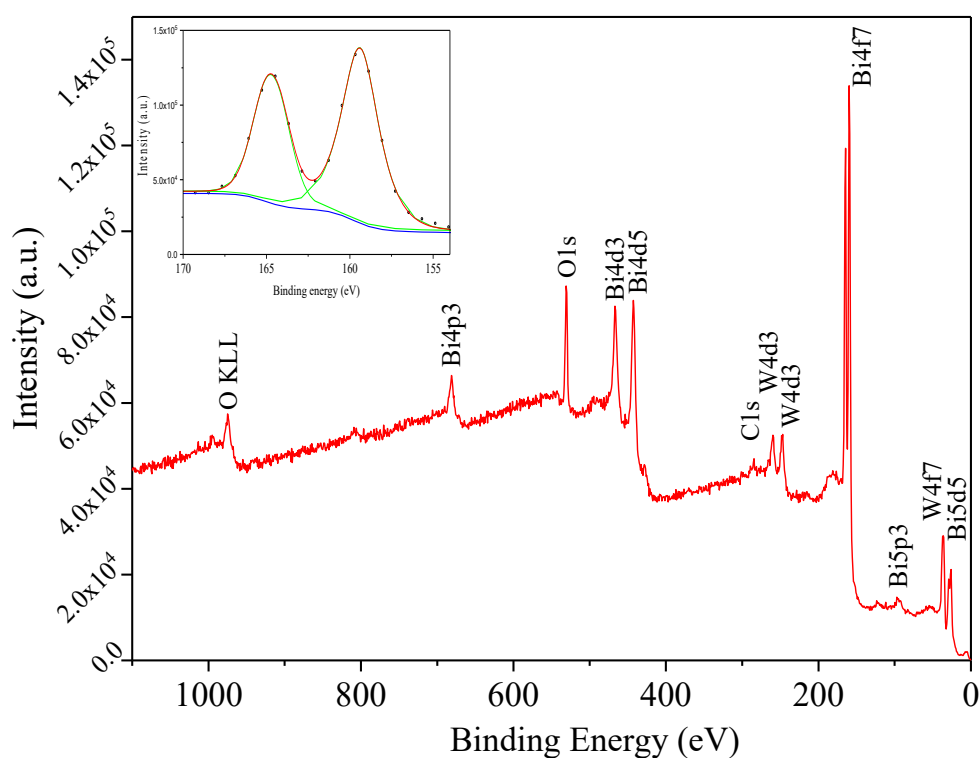**Scheme 2.** Schematic illustration of the growth process of the flower-like Bi_2WO_6 microspheres.

Figure 3. XPS survey spectra of the hydrothermally prepared Bi_2WO_6 sample at 200 °C for 24 h. Inset is the zoom of XPS scans over the $Bi_{4f7/2}$ peak in the 154–170 eV region.

The N_2 adsorption–desorption isotherms of the well-organized flower-like (BWO5) and nanoparticles (BWO6) Bi_2WO_6 are presented in Figure 4. According to IUPAC classification, it can be seen that the isotherm shape for both samples exhibited a typical type IV isotherm with a clear hysteresis loop H3, suggesting the presence of mesopores in the size range of 2–50 nm [37].The insets show the Barrett–Joyner–Halenda (BJH) pore-size distributions and present the evidence for the

existence of mesopores (2–50 nm). Table 3 summarizes the BET specific surface areas (SSA) and the pore volumes of BWO5 and BWO6.
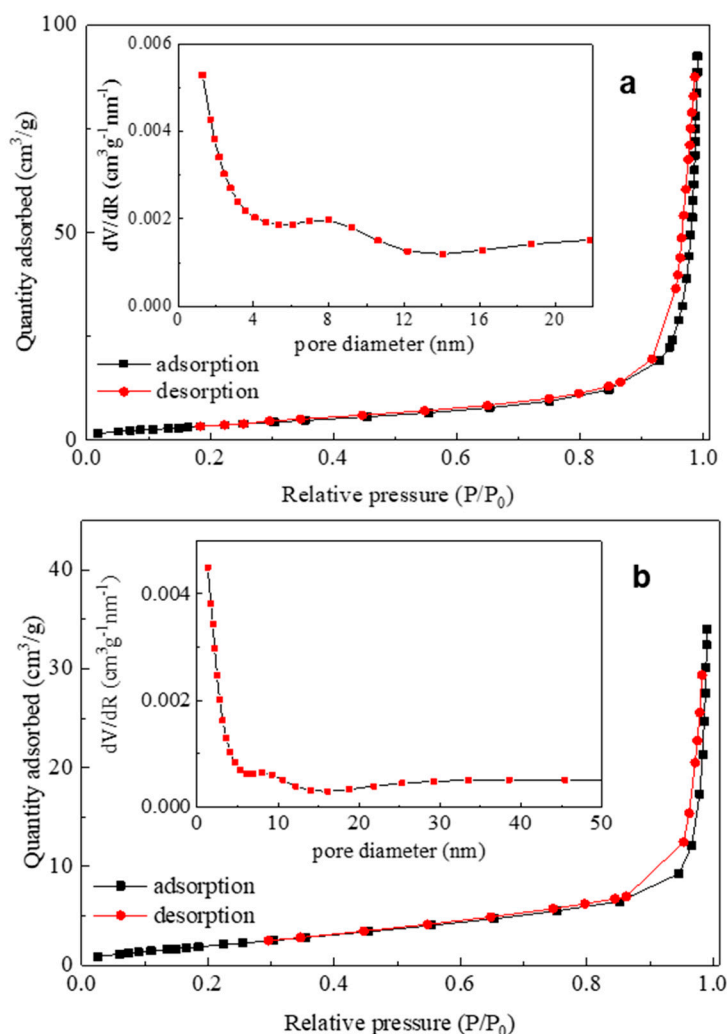

Figure 4. N$_2$ adsorption–desorption isotherm of the samples: (**a**) flower-like Bi$_2$WO$_6$, (**b**) nanoparticle Bi$_2$WO$_6$. The insert shows the pore size distribution.

Table 3. Brunauer–Emmett–Teller (BET) parameters of the Bi$_2$WO$_6$ samples at various temperatures.

Samples	Surface Areas (m^2 g^{-1})	Total Pore Volumes (cm^3 g^{-1})
BWO5	14.475	0.142
BWO6	6.87	0.0532

3.2. E. Coli Inactivation Kinetics: Effect of the Bacterial Concentration, Amount of Catalyst, Light Dose, and Applied Light Wavelength

Figure 5 shows the complete bacterial inactivation mediated by the BWO5 being faster under low-intensity simulated solar light, compared to the other samples. The *E. coli* inactivation was 95% after 2 h. The effectiveness of a disinfection process resides in the time necessary to inactivate a determined percentage of bacteria. In the Chick–Watson model [38,39], the simplest inactivation model, the inactivation rate shown in Figure 5 is seen to be dependent on the residual bacteria after each specific time during the inactivation process and this allows comparing the effect of the different Bi$_2$WO$_6$ samples. Neither irradiation in the absence of Bi$_2$WO$_6$ (photolysis) nor runs in the presence of

this catalyst in the dark lead to bacterial inactivation of up to 4 h. The latter provides the proof that Bi_2WO_6 is not toxic to *E. coli* and a photocatalytic process is required for their inactivation. As the treatment time increased, the photocatalytic process became more effective, owing to the formation of hierarchical flower-like Bi_2WO_6 microspheres and loss of aggregates and the higher crystallite size. Nevertheless, the nanoparticles (BWO6), which presented lower specific surface area than BWO5, led to lower inactivation rates. The pseudo first-order rates of the Bi_2WO_6 samples during flower-like development (BWO1 and BWO5) compared with Bi_2WO_6 nanoparticles (BWO6) are given in the supplementary material, Figure S3. The pseudo first-order rate constants (k_{app}) of the BWO1, BWO5, and BWO6 were estimated to be 0.0331 min^{-1}, 0.0488 min^{-1}, and 0.0195 min^{-1}, respectively. As can be seen, the photocatalytic inactivation of bacteria mediated by as-developed flower-like Bi_2WO_6 (BWO5) is around 2.5 times faster compared with nanoparticles.
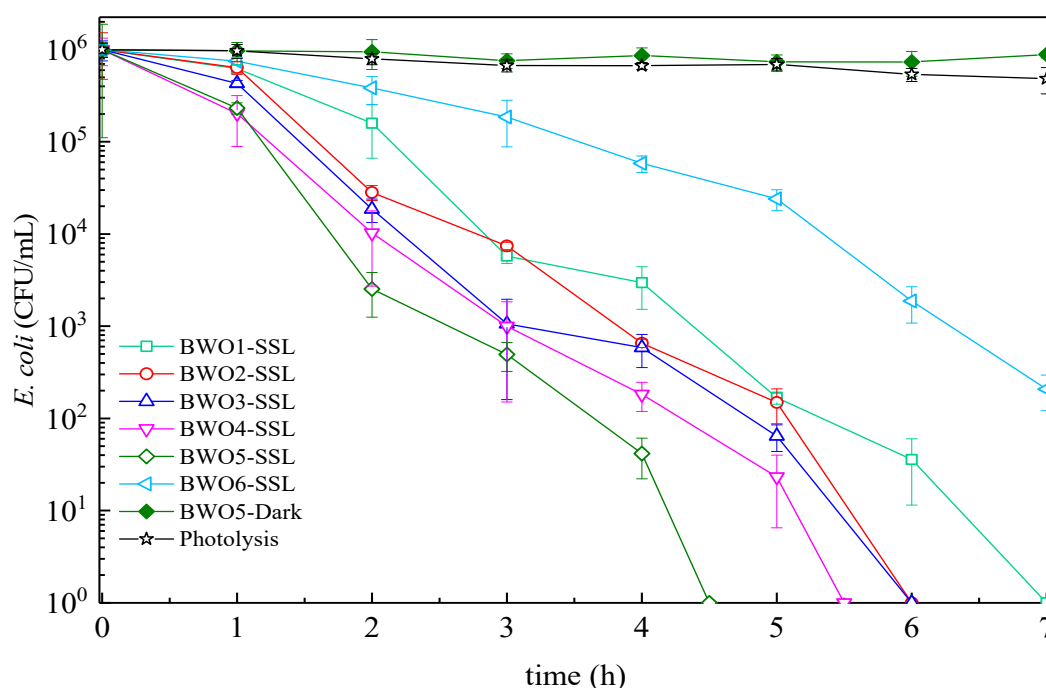

Figure 5. Photocatalytic inactivation of *Escherichia coli* in aqueous dispersions on different Bi_2WO_6 samples in the dark and under simulated solar light (SSL). Experimental conditions: [Catalyst]$_0$ = 0.2 g/L, [bacteria]$_0$ = 2 × 10^6 Colony Forming Units (CFU)/mL and light intensity: 48 mW/cm^2.

The photoluminescence spectrum of the prepared catalysts was used as a practical method to verify the separation efficiency of photo-generated electron–hole pairs in the semiconductors. Generally, a lower photoluminescence (PL) intensity represents a lower recombination rate of photo-generated charge carriers. The photoluminescence (PL) spectra of the Bi_2WO_6 samples during the flower-like development (BWO1 and BWO5) in comparison with Bi_2WO_6 nanoparticles (BWO6) is shown in Figure 6. The wide absorption-band was observed between 350 nm and 600 nm which is due to the Bi_2WO_6 electron-hole recombination giving rise to the free and bound-exciton luminescence [40]. The PL spectra of the as-synthesized samples through flower-like development (BWO1 and BWO5) exhibited significantly decreased PL intensity related to that of the Bi_2WO_6 nanoparticles. It could be ascribed that the recombination of photo-generated charge carriers is greatly inhibited in the hierarchically flower-like composed of nanosheets. Hence, the efficient separation of photo-generated electron–hole pairs and rapid transfer of electrons to the surface of crystal would be obtained. Moreover, the lower PL-intensity bands shown in BWO5 reflected a higher crystallinity in comparison with BWO1, allowing a lower amount of crystal defects, leading to a higher electron-hole separation and an

increased photocatalytic activity [41], a fact that corroborates with the faster inactivation of bacteria (Figure S3).
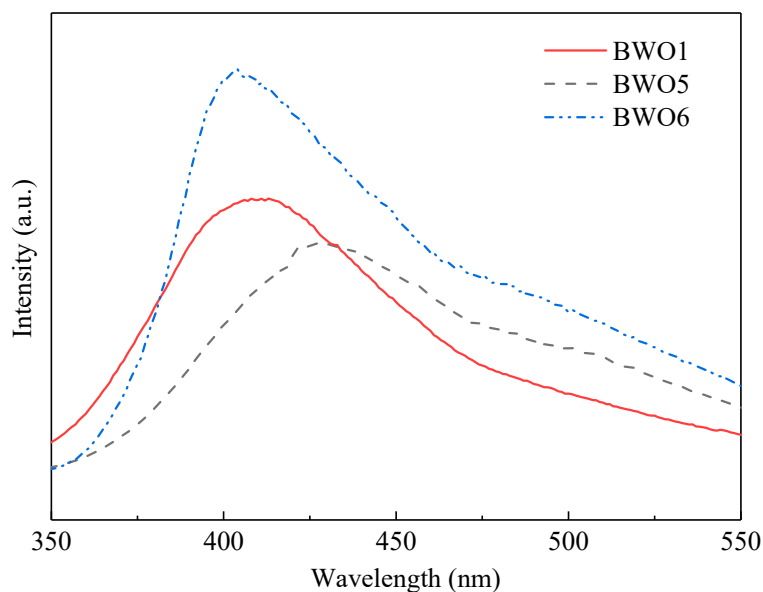

Figure 6. Photoluminescence (PL) spectroscopy of the synthesized samples at different conditions. BWO1: 12 h, 160 °C. BWO5, 24 h, 200 °C. BWO6: 24 h, 200 °C. pH = 10.

Following, the effects of initial catalyst or bacterial concentration were studied, and the results are summarized in Figure 7. The effect of the Bi_2WO_6 concentration on *E. coli* inactivation is shown in Figure 7a. Although increasing Bi_2WO_6 concentration of up to 0.2 mg/mL resulted in higher inactivation rates, increasing the catalyst concentration to 0.4 mg/mL resulted in a slower bacterial inactivation kinetics, most possibly due to a loss in surface area by catalyst agglomeration (particle–particle interactions), as well as a decrease in the penetration of the photon flux by the solution opacity, thereby decreasing the photocatalytic inactivation rate [42]. The effect of the initial concentration on the *E. coli* kinetics mediated by Bi_2WO_6 catalysts is presented in Figure 7b, showing a delay in the time necessary for bacterial inactivation at higher bacterial concentrations. Although this effect can be ascribed to the exhaustion of surface active sites due to opacity in solution [43], we note here that in absolute numbers, the higher the amount of bacteria in solution, the higher the number of available bacteria (for inactivation). Hence, by calculating the amount of cells inactivated in 4 h per mg of catalyst and per minute, we get 2075, 208, and 21 cells min^{-1} mg^{-1} for 10^8, 10^7, and 10^6, respectively. As a result, we report that this catalyst can effectively disinfect higher amounts of microorganisms, albeit in a higher residence time.
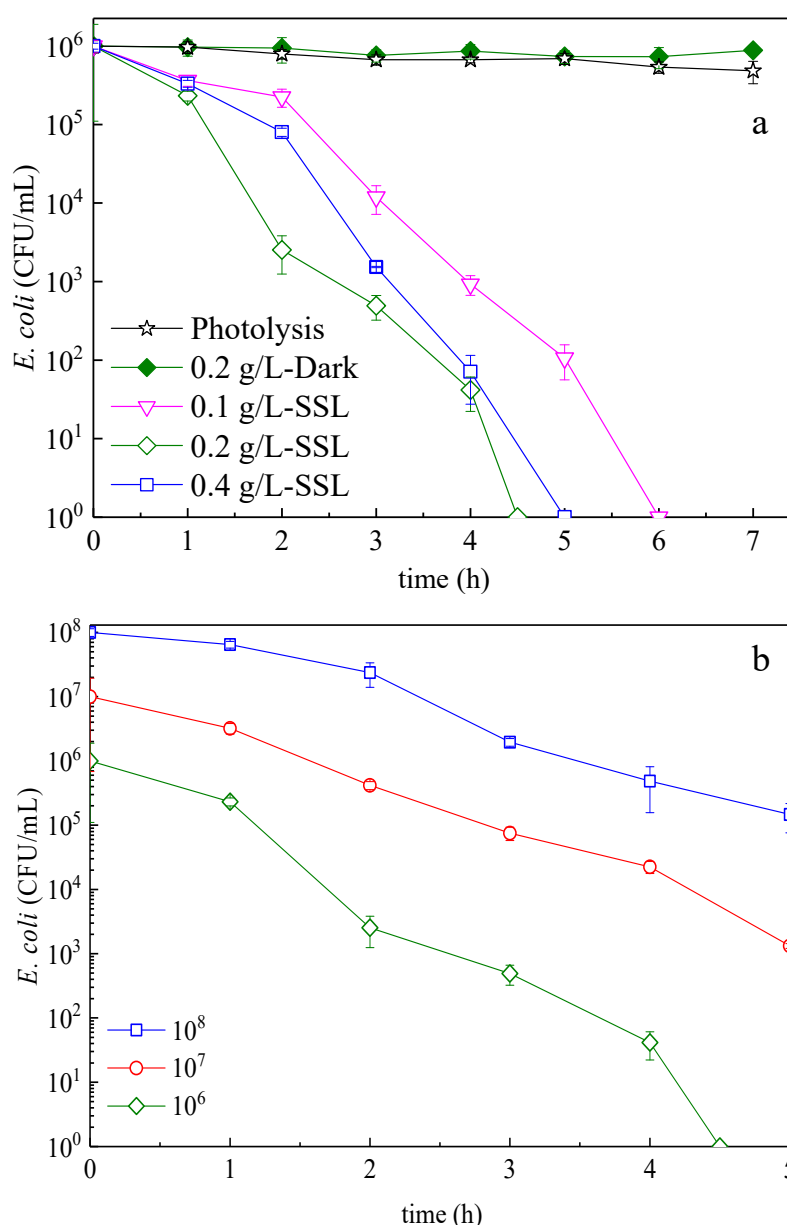
Figure 7. Effect of catalyst and bacterial concentration on inactivation kinetics. (**a**) *E. coli* survival on Bi$_2$WO$_6$ samples in the dark and under low intensity solar simulated light. Experimental conditions: (bacteria)$_0$ = 2 × 10^6 CFU/mL and light intensity: 48 mW/cm^2. (**b**) Initial concentration of *E. coli* (CFU/mL) effects on the bacterial inactivation kinetics mediated by Bi$_2$WO$_6$ (200 °C for 4 h) under low intensity solar simulated light. Experimental conditions: (Catalyst)$_0$ = 0.2 g/L and light intensity: 48 mW/cm^2.

Next up in the operational parameters investigation, we assessed the possibility of photonic limitation or saturation of the system. As such, Figure 8a,b shows the effects of the light intensity and composition (UVA–vis or Vis only) on the bacterial degradation kinetics. A higher light dose accelerated the bacterial inactivation because of a higher amount of charges generated in the semiconductor during bacterial disinfection under band-gap irradiation (Figure 8a), since the direct inactivation by light was previously excluded. Figure 8 b illustrates that under visible light, a solution containing 0.2 g/L of Bi$_2$WO$_6$ was still efficiently inactivating bacteria and was more effective compared to commercial TiO$_2$ P25 Degussa (used as reference). These results come from the optical absorption of up to ~450 nm in the visible region by Bi$_2$WO$_6$, which is significantly wider than that of TiO$_2$ P25 Degussa with an

absorption of up to 387 nm for the 20 nm particles, making up the bulk of this mixed TiO_2 P25 Degussa rutile–anatase [44].
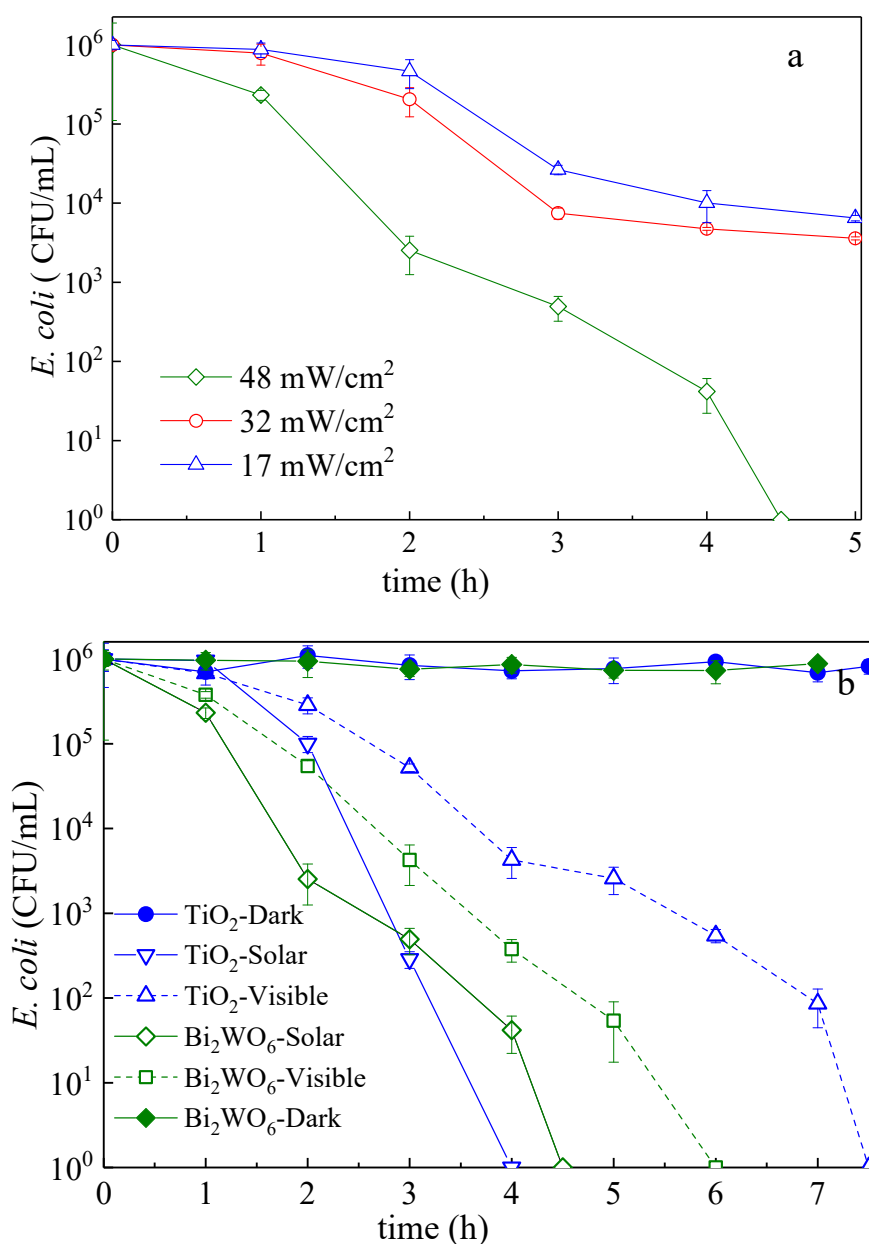

Figure 8. Effect of light irradiance and composition on inactivation kinetics. (**a**) *E. coli* inactivation on Bi_2WO_6 (200 °C for 24 h) under different solar light irradiation intensities. (**b**) *E. coli* inactivation mediated by Bi_2WO_6 (200 °C for 24 h) and TiO_2 under low intensity solar simulated (48 mW/cm^2) and visible light (38 mW/cm^2). Experimental conditions: $(Catalyst)_0 = 0.2$ g/L and $(bacteria)_0 = 2 \times 10^6$ CFU/mL.

3.3. Mechanistic Interpretation: ROS-Species Involvement, Interfacial Charge Transfer, and Catalyst Reuse During Bacterial Inactivation

The reactive oxygen species (ROS) such as $\cdot OH$, $O_2{}^{\cdot-}$, and vb (h^+) play a pivotal role in the photo-degradation of organic pollutants and bacterial inactivation [22,45–47]. To determine the main ROS followed by the photodegradation mechanism, appropriate radical-scavengers such as isopropanol ($\cdot OH$ scavenger), sodium oxalate (a vbh^+ hole scavenger), and superoxide dismutase ($O_2{}^{\cdot-}$ scavenger) were used in the present study. Figure 9 depicts the results of scavenging experiments mediated by the

optimized flower-like Bi_2WO_6 (BWO5). The photocatalytic bacterial inactivation could be remarkably suppressed by the addition of isopropanol and sodium oxalate. It is very likely that ˙OH and h^+ intervene jointly in the bacterial inactivation. Meanwhile, the addition of SOD ($O_2^{˙−}$ scavenger) inhibits the bacterial inactivation to a smaller degree compared to vb(h^+) and the ˙OH-radical as shown in Figure 9, traces (a) and (b).
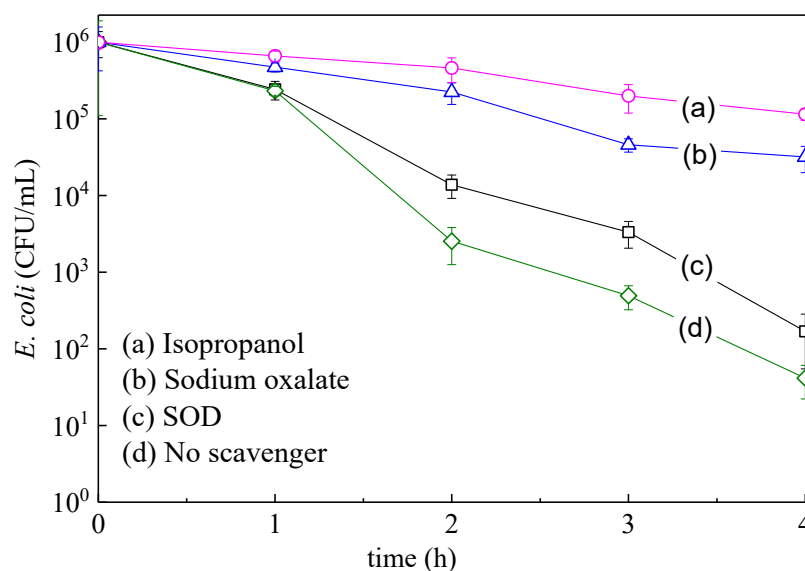

Figure 9. Effect of the scavengers during *E. coli* inactivation on Bi_2WO_6 under solar simulated light for (a) isopropanol as OH-radical scavenger, (b) sodium oxalate a hole vb(h^+) scavenger, (c) superoxide dismutase (SOD) as an O_2^- scavenger, (d) no scavenger. Runs under low intensity solar simulated light (48 mW/cm^2). The solutions contained Bi_2WO_6 (0.2 g/L) and scavenger concentration of 0.1 mM.

The possible reaction mechanism for the inactivation of *E. coli* mediated by Bi_2WO_6 can be proposed as the following, which is shown in Scheme 3. Under visible-light irradiation, the photo-excitation of Bi_2WO_6 implies the transfer of an electron from the valence band (Equation (6)).

$$Bi_2WO_6 + hv \rightarrow e^-(CB) + h^+(VB). \tag{6}$$
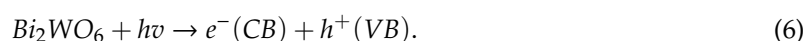
As mentioned before, the valence band of Bi_2WO_6 is a hybrid band made up by the O2p and Bi6s orbitals. Under light irradiation, the O2p and Bi6s hybrid orbitals increase the charge transfer in the W5d orbitals of Bi_2WO_6. This moves the valence band (VB) potential to a more positive potential energy narrowing the band-gap and inducing a higher photocatalytic activity [48].

Based on the references, CB and VB potentials of Bi_2WO_6 are 3.08 and 0.36 eV, respectively [49,50]. The redox potential for the dissolved oxygen/superoxide couple (E^0 (O_2/$O_2^{˙−}$)), O_2/$HO_2^˙$, and OH^-/˙OH are −0.33 eV, −0.046 eV, and 1.98 eV vs NHE [49], respectively. Comparing the band edge energy level of Bi_2WO_6 with the redox potentials of ROS, it is obvious that the excited holes in the valence band of Bi_2WO_6 were sufficiently more positive than that of OH^-/˙OH, suggesting that the photogenerated holes on the surface of Bi_2WO_6 could react with OH^-/H_2O to form "non-selective" ˙OH radicals (Equation (7)). However, the conduction band edge potential of Bi_2WO_6, which is more positive than the standard redox potential of O_2/$O_2^{˙−}$ and O_2/$HO_2^˙$, cannot directly reduce O_2 to $O_2^{˙−}$ or $HO_2^˙$. As shown in Figure 9, the bacterial inactivation is reduced in the presence of SOD-scavengers, which confirms the presence of the $HO_2^˙$ radicals. Considering the redox potential of O_2/H_2O_2 = +0.682 eV vs NHE [51], H_2O_2 seems to be generated initially (Equation (8)) which is followed by the formation of different species according to the relations 9–10 in the photocatalytic reaction. It is worth noting that the powerful hole can directly attack bacteria cells in the photocatalytic oxidation process, which was also confirmed by the hole scavenger [45,52].
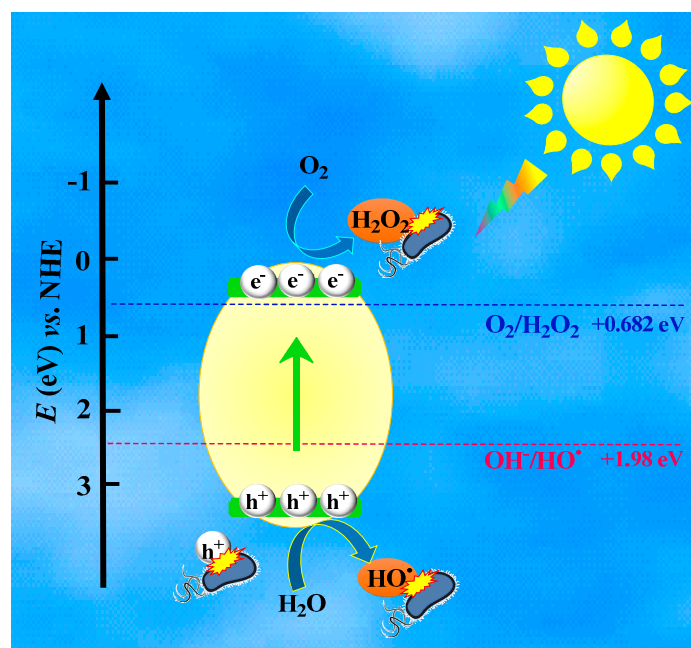
Scheme 3. Schematic diagram showing the photocatalytic inactivation of bacteria on the Bi_2WO_6.

$$h^+(VB) + H_2O \rightarrow HO\bullet + H^+, \tag{7}$$

$$O_2 + 2H^+ + 2e^- \rightarrow H_2O_2, \tag{8}$$

$$H_2O_2 + e^- \rightarrow OH\bullet + OH^-, \tag{9}$$

$$H_2O_2 + h^+ \rightarrow O_2^-\bullet + 2H^+ \ \ or \ \ HO_2^-\bullet + H^+. \tag{10}$$
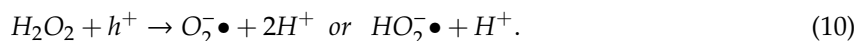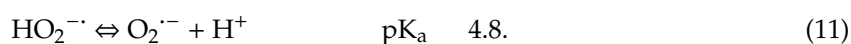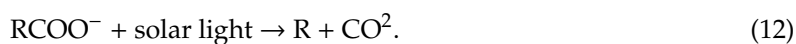
Figure 10 shows the variation of the interfacial potential and the local pH shift under simulated solar light. At pH ~6, the bacterial inactivation preferentially proceeds via the $O_2^{\bullet-}$ species over $HO_2^{-\bullet}$ as shown in Equation (11) and Figure 9, trace (c).

$$HO_2^{-\bullet} \Leftrightarrow O_2^{\bullet-} + H^+ \qquad\qquad pK_a \quad 4.8. \tag{11}$$

The initial pH at time zero in Figure 10 was observed to decrease slightly from 6.0 to 5.9 within four hours of irradiation. The initial pH of 6.0 in this figure is seen to decrease drastically to 5.4 after 8000 s due to the concomitant production of long-lived intermediates carboxylic acids, owing to the degradation of the bacterial membrane. The interface potential is shown to drastically drop within 8000 s (2.2 h) when the bacterial reduction is reduced by 99.90%, which is equivalent to 3 logs as shown in Figure 5. The interface potential recovers to its initial value as shown in Figure 10 after the inactivation of bacteria [52]. The recovery to the initial pH-level occurs when the intermediate acids are mineralized to CO_2 by the photo-Kolbe reaction according to Equation (12) [53,54].
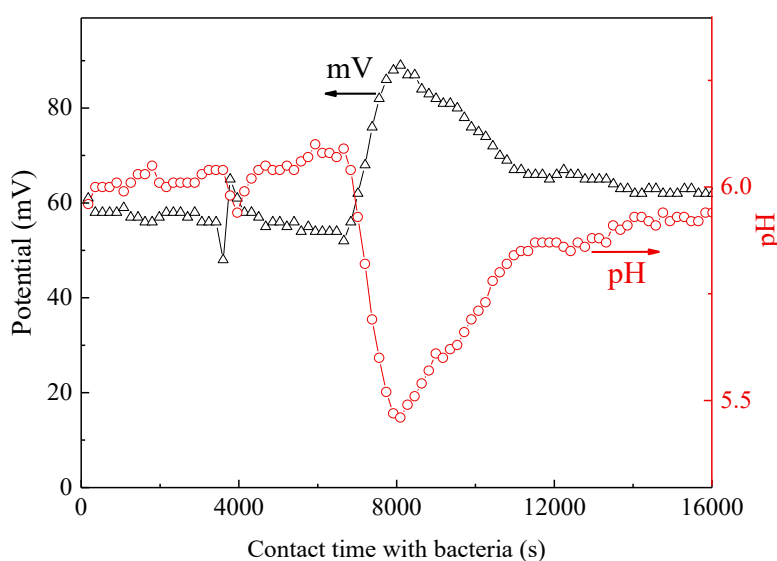
$$RCOO^- + solar\ light \rightarrow R + CO^2. \tag{12}$$

Figure 10. Evolution of the interfacial potential and local pH of an *E. coli* suspension in contact with Bi$_2$WO$_6$ under low intensity light irradiation (48 mW/cm^2). Catalyst concentration 0.2 g/L.

Finally, we provide the evidence for synthesizing a stable Bi$_2$WO$_6$ flower-like photocatalyst by a repetitive inactivation of a *E. coli* test, which results are shown in Figure 11. In order to evaluate the bacterial inactivation after each cycle, the pseudo first-order rate constants (*kapp*) were calculated and are reported in Table 4. The recycled sample used in Figure 11 was thoroughly washed after each cycle. Practically, no loss of bacterial inactivation was observed. These results show the stable repetitive bacterial inactivation mediated by flower-like Bi$_2$WO$_6$ up to five cycles and confirm the potential for the practical application of this photocatalyst in *E. coli* inactivation.
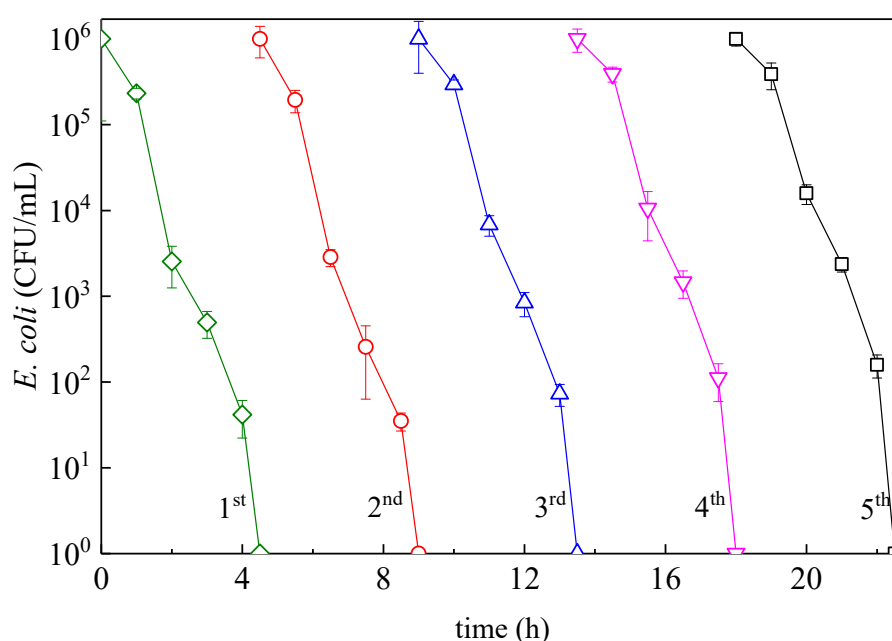

Figure 11. Reusability of flower-like Bi$_2$WO$_6$ under low intensity solar simulated light (48 mW/cm^2). Solution parameters: (Catalyst)$_0$ = 0.2 g/L and (bacteria)$_0$ = 2 × 10^6 CFU/mL.

Table 4. Pseudo first-order rate constants (k_{app}) for *E. coli* inactivation under different conditions consistent with Figure 11.

Cycle Number	k_{app} (min^{-1})
First	0.0488 ± 0.005
Second	0.0494 ± 0.004
Third	0.0484 ± 0.005
Fourth	0.0480 ± 0.006
Fifth	$0.0471 + 0.007$

4. Conclusions

In the present study, Bi_2WO_6 flower-like samples were prepared at 200 °C attaining a high crystallinity and led a low amount of crystal by hydrothermal growth in acetic acid media. By SEM, XRD, XPS, and PL analysis, the properties of the flower-like Bi_2WO_6 samples and nanoparticles were investigated. These catalysts resulted in effective bacterial inactivation even under visible light and were faster than TiO_2. In addition to higher SSA of flower-like Bi_2WO_6, its lower PL intensity leads to lower recombination of photo-generated electron–hole pairs as a consequence of more efficient photocatalytic activity. The photocatalytic inactivation of bacteria mediated by as-developed flower-like Bi_2WO_6 (BWO5) is around 2.5 times faster when compared with nanoparticles. The samples under light lead to effective Bi_2WO_6 charge separation and the generation of ROS inducing bacterial inactivation. The intermediate ROS species produced by Bi_2WO_6 were identified by the use of the appropriate scavengers, and the ˙OH-radical was identified to be the dominant inactivation mechanism. Finally, the stable performance of the synthesized catalyst during recycling indicates its robustness and may suggest practical application potential.

Supplementary Materials: The following are available online at http://www.mdpi.com/2073-4441/12/4/1099/s1, **Figure S1.** SUNTEST solar simulator light wavelength emission spectrum (Manufacturer: Atlas, CPS+/CPS Instruments Brochure), **Figure S2.** Transmittance of the polymethylmethacrylate filter used to block UV light, **Figure S3.** Pseudo first-order rates of the Bi_2WO_6 samples during flower-like development (BWO1 and BWO5) compared with Bi2WO6 nanoparticles (BWO6).

Author Contributions: Conceptualization, M.K., S.G., C.P., S.R., and J.K.; methodology, M.K., S.G., S.R., J.K., and C.P.; software, M.K.; validation, M.K., S.G., S.R., and J.K.; investigation, M.K.; resources, C.P., F.K., and K.R.; writing—original draft preparation, M.K., F.K., K.R., S.R., J.K., S.G., and C.P.; writing—review & editing, M.K. and S.G.; visualization, M.K.; supervision, F.K., K.R., S.R., J.K., and C.P.; project administration, C.P., F.K., and K.R.; funding acquisition, S.G., C.P., F.K., and K.R. All authors have read and agreed to the published version of the manuscript.

Conflicts of Interest: The authors declare no conflict of interest.

References

1. Giannakis, S.; Jovic, M.; Gasilova, N.; Pastor Gelabert, M.; Schindelholz, S.; Furbringer, J.M.; Girault, H.; Pulgarin, C. Iohexol degradation in wastewater and urine by UV-based Advanced Oxidation Processes (AOPs): Process modeling and by-products identification. *J. Environ. Manag.* **2017**, *195*, 174–185. [CrossRef] [PubMed]

2. Chong, M.N.; Jin, B.; Chow, C.W.K.; Saint, C. Recent developments in photocatalytic water treatment technology: A review. *Water Res.* **2010**, *44*, 2997–3027. [CrossRef] [PubMed]

3. Pelaez, M.; Nolan, N.T.; Pillai, S.C.; Seery, M.K.; Falaras, P.; Kontos, A.G.; Dunlop, P.S.M.; Hamilton, J.W.J.; Byrne, J.A.; O'Shea, K.; et al. A review on the visible light active titanium dioxide photocatalysts for environmental applications. *Appl. Catal. B Environ.* **2012**, *125*, 331–349. [CrossRef]

4. Campoccia, D.; Montanaro, L.; Arciola, C.R. A review of the biomaterials technologies for infection-resistant surfaces. *Biomaterials* **2013**, *34*, 8533–8554. [CrossRef]

5. Giannakis, S.; Merino Gamo, A.I.; Darakas, E.; Escalas-Cañellas, A.; Pulgarin, C. Impact of different light intermittence regimes on bacteria during simulated solar treatment of secondary effluent: Implications of the inserted dark periods. *Sol. Energy* **2013**, *98*, 572–581. [CrossRef]

6. Giannakis, S.; Darakas, E.; Escalas-Cañellas, A.; Pulgarin, C. Environmental considerations on solar disinfection of wastewater and the subsequent bacterial (re)growth. *Photochem. Photobiol. Sci.* **2015**, *14*, 618–625. [CrossRef]

7. Byrne, J.A.; Dunlop, P.S.M.; Hamilton, J.W.J.; Fernández-Ibáñez, P.; Polo-López, I.; Sharma, P.K.; Vennard, A.S.M. A Review of Heterogeneous Photocatalysis for Water and Surface Disinfection. *Molecules* **2015**, *20*, 5574–5615. [CrossRef]

8. Rizzo, L.; Della Sala, A.; Fiorentino, A.; Li Puma, G. Disinfection of urban wastewater by solar driven and UV lamp–TiO$_2$ photocatalysis: Effect on a multi drug resistant Escherichia coli strain. *Water Res.* **2014**, *53*, 145–152. [CrossRef]

9. Carré, G.; Hamon, E.; Ennahar, S.; Estner, M.; Lett, M.C.; Horvatovich, P.; Gies, J.P.; Keller, V.; Keller, N.; Andre, P. TiO$_2$ photocatalysis damages lipids and proteins in Escherichia coli. *Appl. Environ. Microbiol.* **2014**, *80*, 2573–2581. [CrossRef]

10. Ouyang, K.; Dai, K.; Walker, S.L.; Huang, Q.; Yin, X.; Cai, P. Efficient photocatalytic disinfection of Escherichia coli O157:H7 using C70-TiO$_2$hybrid under visible light irradiation. *Sci. Rep.* **2016**, *6*, 1–8. [CrossRef]

11. Nakata, K.; Fujishima, A. TiO$_2$ photocatalysis: Design and applications. *J. Photochem. Photobiol. C Photochem. Rev.* **2012**, *13*, 169. [CrossRef]

12. Zhang, L.; Wang, W.; Chen, Z.; Zhou, L.; Xu, H.; Zhu, W. Fabrication of flower-like Bi$_2$WO$_6$superstructures as high performance visible-light driven photocatalysts. *J. Mater. Chem.* **2007**, *17*, 2526–2532. [CrossRef]

13. Zhang, L.; Wang, H.; Chen, Z.; Wong, P.K.; Liu, J. Bi$_2$WO$_6$ micro/nano-structures: Synthesis, modifications and visible-light-driven photocatalytic applications. *Appl. Catal. B Environ.* **2011**, *106*, 1–13. [CrossRef]

14. Saison, T.; Gras, P.; Chemin, N.; Chanéac, C.; Durupthy, O.; Brezová, V.; Colbeau-Justin, C.; Jolivet, J.P. New insights into Bi$_2$WO$_6$ properties as a visible-light photocatalyst. *J. Phys. Chem. C* **2013**, *117*, 22656–22666. [CrossRef]

15. Zhang, L.; Zhu, Y. A review of controllable synthesis and enhancement of performances of bismuth tungstate visible-light-driven photocatalysts. *Catal. Sci. Technol.* **2012**, *2*, 694–706. [CrossRef]

16. Chen, M. Degradation of Antibiotic Norfloxacin by Solar Light/Visible Light-Assisted Oxidation Processes in Aqueous Phase. Ph.D. Thesis, The Hong Kong Polytechnic University, Hong Kong, China, 2013.

17. Shang, Y.; Cui, Y.; Shi, R.; Yang, P. Effect of acetic acid on morphology of Bi$_2$WO$_6$with enhanced photocatalytic activity. *Mater. Sci. Semicond. Process.* **2019**, *89*, 240–249. [CrossRef]

18. Zhang, Q.; Chen, J.; Xie, Y.; Wang, M.; Ge, X. Inductive effect of poly (vinyl pyrrolidone) on morphology and photocatalytic performance of Bi$_2$WO$_6$. *Appl. Surf. Sci.* **2016**, *368*, 332–340. [CrossRef]

19. Shen, R.; Jiang, C.; Xiang, Q.; Xie, J.; Li, X. Surface and interface engineering of hierarchical photocatalysts. *Appl. Surf. Sci.* **2018**, *471*, 43–87. [CrossRef]

20. Li, C.; Chen, G.; Sun, J.; Rao, J.; Han, Z.; Hu, Y.; Zhou, Y. A Novel Mesoporous Single-Crystal-Like Bi$_2$WO$_6$with Enhanced Photocatalytic Activity for Pollutants Degradation and Oxygen Production. *ACS Appl. Mater. Interfaces* **2015**, *7*, 25716–25724. [CrossRef]

21. Ren, J.; Wang, W.; Zhang, L.; Chang, J.; Hu, S. Photocatalytic inactivation of bacteria by photocatalyst Bi$_2$WO$_6$ under visible light. *Catal. Commun.* **2009**, *10*, 1940–1943. [CrossRef]

22. Helali, S.; Polo-López, M.I.; Fernández-Ibáñez, P.; Ohtani, B.; Amano, F.; Malato, S.; Guillard, C. Solar photocatalysis: A green technology for E. coli contaminated water disinfection. Effect of concentration and different types of suspended catalyst. *J. Photochem. Photobiol. A Chem.* **2014**, *276*, 31–40. [CrossRef]

23. Amano, F.; Nogami, K.; Ohtani, B. Visible Light-Responsive Bismuth Tungstate Photocatalysts: Effects of Hierarchical Architecture on Photocatalytic Activity. *J. Phys. Chem* **2009**, *113*, 1536–1542. [CrossRef]

24. Porras, J.; Giannakis, S.; Torres-Palma, R.A.; Fernandez, J.J.; Bensimon, M.; Pulgarin, C. Fe and Cu in humic acid extracts modify bacterial inactivation pathways during solar disinfection and photo-Fenton processes in water. *Appl. Catal. B Environ.* **2018**, *235*. [CrossRef]

25. Marjanovic, M.; Giannakis, S.; Grandjean, D.; de Alencastro, L.F.; Pulgarin, C. Effect of MM Fe addition, mild heat and solar UV on sulfate radical-mediated inactivation of bacteria, viruses, and micropollutant degradation in water. *Water Res.* **2018**, *140*, 220–231. [CrossRef]

26. Zhang, C.; Zhu, Y. Synthesis of Square Bi2WO6 Nanoplates as High-Activity Visible-Light-Driven Photocatalysts, Chem. *Chem. Mater.* **2005**, *17*, 3537–3545. [CrossRef]

27. Liang, Y.; Shi, J.; Fang, B. Synthesis and electrochemical performance of bismuth tungsten oxides with different composition and morphology. *Chem. Phys. Lett.* **2019**, *716*, 112–118. [CrossRef]

28. Guan, J.; Liu, L.; Xu, L.; Sun, Z.; Zhang, Y. Nickel flower-like nanostructures composed of nanoplates: One-pot synthesis, stepwise growth mechanism and enhanced ferromagnetic properties. *CrystEngComm* **2011**, *13*, 2636. [CrossRef]

29. Donaldson, J.D.; Knifton, J.F.; Ross, S.D. The fundamental vibrational spectra of the formates of the main group elements. *Spectrochim. Acta* **1964**, *20*, 847–851. [CrossRef]

30. Anderegg, G.; Arnaud-Neu, F.; Delgado, R.; Felcman, J.; Popov, K. Critical evaluation of stability constants of metal complexes of complexones for biomedical and environmental applications (IUPAC Technical Report). *Pure Appl. Chem.* **2005**, *77*, 1445–1495. [CrossRef]

31. Portanova, R.; Lajunen, L.H.J.; Tolazzi, M.; Piispanen, J. Critical evaluation of stability constants for alpha-hydroxycarboxylic acid complexes with protons and metal ions and the accompanying enthalpy changes. Part II. Aliphatic 2-hydroxycarboxylic acids (IUPAC Technical Report). *Pure Appl. Chem.* **2003**, *75*, 495–540. [CrossRef]

32. Briand, G.G.; Burford, N. Coordination Complexes of Bismuth(III) Involving Organic Ligands with Pnictogen or Chalcogen Donors. *Adv. Inorg. Chem.* **2000**, *50*, 285–357.

33. Tang, R.; Su, H.; Sun, Y.; Zhang, X.; Li, L.; Liu, C.; Wang, B.; Zeng, S.; Sun, D. Facile Fabrication of Bi_2WO_6/Ag2S Heterostructure with Enhanced Visible-Light-Driven Photocatalytic Performances. *Nanoscale Res. Lett.* **2016**, *11*, 126. [CrossRef] [PubMed]

34. Xu, X.; Ge, Y.; Wang, H.; Li, B.; Yu, L.; Liang, Y.; Chen, K.; Wang, F. Sol–gel synthesis and enhanced photocatalytic activity of doped bismuth tungsten oxide composite. *Mater. Res. Bull.* **2016**, *73*, 385–393. [CrossRef]

35. Li, W.; Wang, Q.; Huang, L.; Li, Y.; Xu, Y.; Song, Y.; Zhang, Q.; Xu, H.; Li, H. Synthesis and characterization of BN/Bi_2WO_6 composite photocatalysts with enhanced visible-light photocatalytic activity. *RSC Adv.* **2015**, *5*, 88832–88840. [CrossRef]

36. Tang, R.; Su, H.; Sun, Y.; Zhang, X.; Li, L.; Liu, C.; Zeng, S.; Sun, D. Journal of Colloid and Interface Science Enhanced photocatalytic performance in Bi_2WO_6/SnS heterostructures: Facile synthesis, influencing factors and mechanism of the photocatalytic process. *J. Colloid Interface Sci.* **2016**, *466*, 388–399. [CrossRef]

37. Guo, Y.; Zhang, G.; Gan, H.; Zhang, Y. Micro/nano-structured $CaWO_4$/Bi_2WO_6 composite: Synthesis, characterization and photocatalytic properties for degradation of organic contaminants. *Dalton Trans.* **2012**, *41*, 12697. [CrossRef]

38. Chick, H. An Investigation of the Laws of Disinfection. *J. Hyg. (Lond)* **1908**, *8*, 92–158. [CrossRef]

39. Watson, H.E. A Note on the Variation of the Rate of Disinfection with Change in the Concentration of the Disinfectant. *J. Hyg. (Lond)* **1908**, *8*, 536–542. [CrossRef]

40. Sun, X.; Zhang, H.; Wei, J.; Yu, Q.; Yang, P.; Zhang, F. Preparation of point-line Bi_2WO_6@TiO_2 nanowires composite photocatalysts with enhanced UV/visible-light-driven photocatalytic activity. *Mater. Sci. Semicond. Process.* **2016**, *45*, 51–56. [CrossRef]

41. Docampo, P.; Guldin, S.; Steiner, U.; Snaith, H.J. Charge Transport Limitations in Self-Assembled TiO_2 Photoanodes for Dye-Sensitized Solar Cells. *J. Phys. Chem. Lett.* **2013**, *4*, 698–703. [CrossRef]

42. Kh, M.; Reza, A.; Kurny, F.G. Parameters affecting the photocatalytic degradation of dyes using TiO_2: A review. *Appl. Water Sci.* **2017**, *7*, 1569–1578.

43. Adhikari, S.; Banerjee, A.; Eswar, N.K.R.; Sarkar, D.; Madras, G. Photocatalytic inactivation of E. Coli by ZnO-Ag nanoparticles under solar radiation. *RSC Adv.* **2015**, *5*, 51067–51077. [CrossRef]

44. Winkler, J. *Titanium Dioxide: Production, Properties and Effective Usage*; Vincentz Network: Hanover, Germany, 2013; ISBN 9783866308121.

45. Nosaka, Y.; Nosaka, A.Y. Generation and Detection of Reactive Oxygen Species in Photocatalysis. *Chem. Rev.* **2017**, *117*, 11302–11336. [CrossRef] [PubMed]

46. Benabbou, A.K.; Derriche, Z.; Felix, C.; Lejeune, P.; Guillard, C. Photocatalytic inactivation of *Escherischia coli*: Effect of concentration of TiO2 and microorganism, nature, and intensity of UV irradiation. *Appl. Catal. B Environ.* **2007**, *76*, 257–263.

47. Regmi, C.; Joshi, B.; Ray, S.K.; Gyawali, G.; Pandey, R.P. Understanding Mechanism of Photocatalytic Microbial Decontamination of Environmental Wastewater. *Front. Chem.* **2018**, *6*, 33. [CrossRef]

48. Wei, Z.; Zhu, Y.; Kudo, A. *Nanostructured Photocatalysts*; Springer International Publishing: Basel, Switzerland, 2016; ISBN 978-3-319-26077-8.

49. Xu, J.; Wang, W.; Sun, S.; Wang, L. Enhancing visible-light-induced photocatalytic activity by coupling with wide-band-gap semiconductor: A case study on Bi_2WO_6/TiO_2. *Appl. Catal. B Environ.* **2012**, *111–112*, 126–132. [CrossRef]

50. Schneider, J.; Bahnemann, D.; Ye, J.; Puma, G.L.; Dionysiou, D.D. *Photocatalysis*; Royal Society of Chemistry: Cambridge, UK, 2016; ISBN 9781782620419.

51. Wu, D.; Wang, W.; Ng, T.W.; Huang, G.; Xia, D.; Yip, H.Y.; Lee, H.K.; Li, G.; An, T.; Wong, P.K. Visible-light-driven photocatalytic bacterial inactivation and the mechanism of zinc oxysulfide under LED light irradiation. *J. Mater. Chem. A* **2016**, *4*, 1052–1059. [CrossRef]

52. Sherman, I.; Gerchman, Y.; Sasson, Y.; Gnayem, H.; Mamane, H. Disinfection and Mechanistic Insights of Escherichia coli in Water by Bismuth Oxyhalide Photocatalysis. *Photochem. Photobiol.* **2016**, *92*, 826–834. [CrossRef]

53. Kiwi, J.; Nadtochenko, V. New Evidence for TiO_2 Photocatalysis during Bilayer Lipid Peroxidation. *J. Phys. Chem. B* **2004**, *108*, 17675–17684. [CrossRef]

54. Kraeutler, B.; Bard, A.J. Heterogeneous photocatalytic decomposition of saturated carboxylic acids on titanium dioxide powder. Decarboxylative route to alkanes. *J. Am. Chem. Soc.* **1978**, *100*, 5985–5992. [CrossRef]